Review

Heavy Metal-Based Nanoparticles as High-Performance X-Ray Computed Tomography Contrast Agents

Mohammad Yaseen Ahmad , Shuwen Liu , Tirusew Tegafaw , Abdullah Khamis Ali Al Saidi , Dejun Zhao , Ying Liu , Sung-Wook Nam , Yongmin Chang * , Gang Ho Lee *

Posted Date: 23 August 2023

doi: 10.20944/preprints202308.1571.v1

Keywords: heavy metal-based nanoparticles; X-ray attenuation; contrast agents; in vitro phantom imaging; in vivo imaging

Review

Heavy Metal-Based Nanoparticles as High-Performance X-Ray Computed Tomography Contrast Agents

Mohammad Yaseen Ahmad [1,#], Shuwen Liu [1,#], Tirusew Tegafaw [1], Abdullah Khamis Ali Al Saidi [1], Dejun Zhao [1], Ying Liu [1], Sung-Wook Nam [2], Yongmin Chang [2,*] and Gang Ho Lee [1,*]

[1] Department of Chemistry, College of Natural Sciences, Kyungpook National University, Taegu 41566, South Korea; yaseen.knu@gmail.com (M.Y.A.); liushuwen0701@gmail.com (S.L.); tegafawtirusew@yahoo.com (T.T.); abdullah_al_saidi@hotmail.com (A.K.A.A.S.); djzhao.chem@gmail.com (D.Z.); ly1124161@gmail.com (Y.L.)

[2] Department of Molecular Medicine, School of Medicine, Kyungpook National University, Taegu 41944, South Korea; nams@knu.ac.kr (S.-W.N.)

# Equal contribution.

* Correspondence: ychang@knu.ac.kr (Y.C.); ghlee@mail.knu.ac.kr (G.H.L.)

Abstract: Contrast agents developed for X-ray computed tomography (CT) offer extremely valuable tools and techniques in diagnostics *via* contrast enhancements. Heavy metal-based nanoparticles (NPs) can provide high contrast in CT images. These result from a high density of heavy metal atoms with high X-ray attenuation coefficients that exceed that of iodine (I), which is currently used in hydrophilic organic CT contrast agents. Nontoxicity and colloidal stability are vital characteristics in designing heavy metal-based NPs as CT contrast agents. In addition, the particle size must be small for in vivo renal excretion. In vitro phantom imaging studies can provide X-ray attenuation efficiency, which is a critical parameter for CT contrast agents, and the imaging performance of CT contrast agents can be demonstrated *via* in vivo experiments. This review focuses on in vitro and in vivo studies of various heavy metal-based NPs (metal: Au, Pt, Pd, Ag, Ce, Gd, Dy, Ho, Yb, Ta, W, and Bi) and provides an outlook on their use as high-performance CT contrast agents.

Keywords: heavy metal-based nanoparticles; X-ray attenuation; contrast agents; in vitro phantom imaging; in vivo imaging

1. Introduction

Heavy metal-based nanoparticles (NPs) are extremely valuable materials in various areas that utilize their high surface-to-volume ratios and optical, magnetic, antibacterial, and mechanical properties [1–3]. Surface modification can endow them with biocompatibility and colloidal stability for applications in various biomedical areas, such as imaging, cancer therapy, and targeted drug delivery. In particular, they can strongly attenuate X-rays because X-ray attenuation is proportional to atomic number (Z) [4]. Therefore, heavy metal-based NPs can serve as contrast agents in X-ray computed tomography (CT) [5–11].

Contrast agents play an important role in CT because they enable accurate diagnosis and monitoring of diseases *via* contrast enhancements [5]. In addition, they allow the detection of small lesions through increased contrasts. Heavy metal-based NPs have emerged as a promising new class of powerful CT contrast agents because they possess a high density of heavy metal atoms with high X-ray attenuation coefficients.

Conventional iodine (I, Z = 53) CT contrast agents are organic compounds with three iodines per molecule or six iodines per dimeric molecule [12]. They have shown limitations such as short blood circulation times and high injection doses (> 1 mmol/kg) owing to their low imaging sensitivity. High injection doses may lead to possible renal toxicity or side effects [13]. In addition, iodine-based CT contrast agents are randomly dispersed throughout the intravascular and extravascular regions, resulting in confounding CT images [14]. These limitations can be reduced using heavy metal-based

Preprints (www.preprints.org) | NOT PEER-REVIEWED | Posted: 23 August 2023 doi:10.20944/preprints202308.1571.v1

NPs owing to their higher X-ray attenuation and longer blood circulation times. Furthermore, heavy metal-based NPs can be easily surface-modified with targeting molecules which are used to enhance the visibility of specific diseases, organs, and tissues in CT scans, making them excellent candidates for highly sensitive and specific CT contrast agents [15,16].

Biocompatibility, colloidal stability, and renal excretion must be carefully designed to develop heavy metal-based NPs as CT contrast agents [17–19]. Surface modification can be used to improve biocompatibility and colloidal stability. In particular, polyethylene glycol (PEG) as a surface coating can improve blood circulation times [20–22]. The elimination of NPs *via* the renal system is essential because most heavy metals are toxic [23]. This can be achieved *via* the reduction of particle diameter (d) and hydrodynamic diameter (HD) as much as possible (< 3 nm) [18,19].

Various heavy metal-based NPs have been investigated as potential CT contrast agents, including NPs made of palladium (Pd, Z = 46) [24], silver (Ag, Z = 47) [25–28], cerium (Ce, Z = 58) [29,30], gadolinium (Gd, Z = 64) [31–35], dysprosium (Dy, Z = 66) [32,36,37], holmium (Ho, Z = 67) [37–40], ytterbium (Yb, Z = 70) [32,41–46], tantalum (Ta, Z = 73) [32,47–50] , tungsten (W, Z = 74) [51–55], platinum (Pt, Z = 78) [56–63], gold (Au, Z = 79) [64-81], and bismuth (Bi, Z = 83) [32,82-88]. These NPs are overviewed (Table 1) and their performances are compared with those of commercial iodine-based CT contrast agents based on their X-ray attenuation efficiencies and in vivo performance.

2. Basic Principles of CT Contrast Agents

CT is a medical imaging technique that provides detailed cross-sectional images of the body using differential X-ray attenuation properties of tissues, bones, and organs [89]. CT is especially useful for imaging bones and hardened diseases because soft tissues made of light elements (C, H, O, N, etc.) weakly attenuate X-rays. Using CT contrast agents, soft tissues, organs, and blood vessels can also be imaged. As shown in Figure 1, linear X-ray attenuation coefficients of heavy metal atoms are higher than that of iodine [4]. Therefore, heavy metal-based NPs may offer more effective CT contrast agents than iodine-based CT contrast agents.

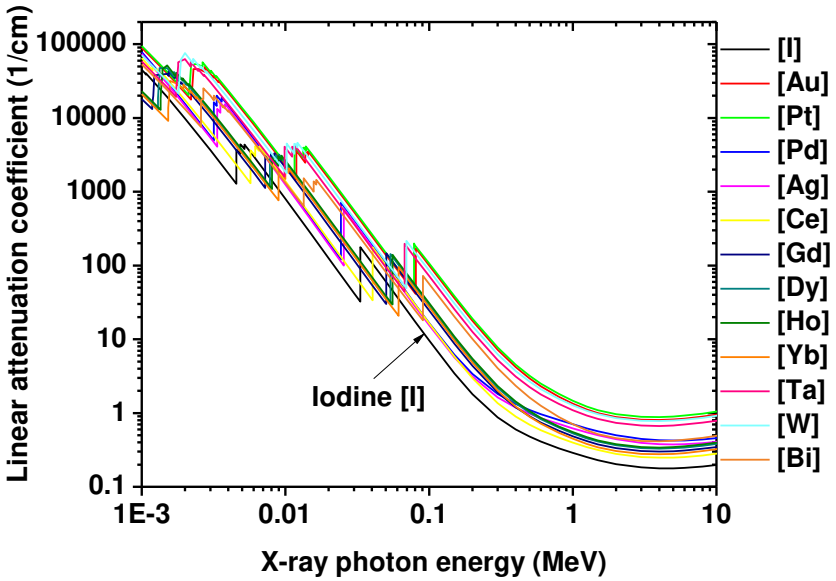

Figure 1. Linear X-ray attenuation coefficients [4] of heavy metal atoms and I versus X-ray photon energy.

Table 1. X-ray attenuation efficiency (η) of various heavy-metal based NPs, nanorods, and nanosheets.

Metal	Z [1]	Chemical formula	Coating ligand	Morphology	Size[2]	η (HU/mM)	Tube voltage (kVp)	Ref.

Preprints (www.preprints.org) | NOT PEER-REVIEWED | Posted: 23 August 2023 doi:10.20944/preprints202308.1571.v1

Pd	46	FePd	Cysteamine	Spherical	3.4	2.6	-	24
Ag	47	Ag	Generation-5 poly(amido-amine) dendrimer	Spherical	8.8 12.4 16.1 23.2	~2.4 ~4.6 ~7.2 ~4.0	80	25
		Ag	Hyaluronic acid	Spherical	~10	3.5	-	26
		Ag_2S	Glutathione	Spherical	2.3, 3.1, 5.1	~3.5 ~2.7 ~2.3 ~1.9 (nearly particle size independent	80 100 120 140	27
		Ag	Bovine serum albumin	Spherical	5.8	5.7	-	28
Ce	58	CeO_2	Dextran	Spherical	4.8	~6.3 ~4.8 ~3.8 ~3.2	80 100 120 140	29
		CeO_2	Murine serum albumin	Spherical	5.1	-	-	30
Gd	64	Gd_2O_3	$C_8H_4I_3NO_4$	Spherical	2	11.8	70	31
		Gd_2O_3	Polyacrylic acid	Spherical	1.9	5.9	70	32
		$Gd(IO_3)_3 H_2O$	D-glucuronic acid	Mixture of nanosheet & nanorod	nanosheet (110, 750); nanorod (325×150)	~5.1	35	33
		GdF_3:Fe	Polyethylene glycol	Nanorod	51.9×31.3	6.9	120	34
		GdF_3	Polyacrylic acid	Nanoplate	10.6×7.0×4.2	~7.9	60	35
Dy	66	Dy_2O_3	Polyacrylic acid	Spherical	1.8	6.1	70	32
		Dy_2O_3	Polyethyleneimine	Spherical	79–102	~5	120	36
		$DyVO_4$	Polyacrylic acid	Spherical	60	4.8	65	37
Ho	67	HoF_3	Polyethylene glycol	Spherical	38	190	120	38
		$BaHoF_5$	Polyethylene glycol	Spherical	7	4.8	80	39
		$NaHoF_4$	Polyethylene glycol	Spherical	3.2	6.9	120	40
		$HoVO_4$	Polyacrylic acid	Spherical	65	4.8	65	37

Preprints (www.preprints.org) | NOT PEER-REVIEWED | Posted: 23 August 2023 doi:10.20944/preprints202308.1571.v1

Yb	70	Yb_2O_3	Polyacrylic acid	Spherical	1.7	6.8	70	32
		Yb_2O_3	D-glucuronic acid	Spherical	2.1	~9.7	70	41
		$BaYbF_5$	-	Spherical	8, 11	~2.7 (8 nm), ~2.6 (11 nm)	70	42
		$BaYbF_5$@SiO_2	-	Spherical	27, 34	~1.8 (27 nm), ~1.2 (34 nm)	70	42
		Yb	3-mercaptopro-pionic acid	Spherical	4.75	~10.4	55	43
		$Yb(OH)CO_3$	-	Spherical	170	~9.0	120	44
		$NaYbF_4$:Er	phospholipid-polyethylene glycol	Spherical	40	~9.9	120	45
		Yb_2O_3:Er	Polyethylene glycol	Spherical	170	10.0	120	46
Ta	73	$NaTaO_3$	Polyacrylic acid	Spherical	1.5	10.3	70	32
		TaO_x	Polyethylene glycol-silane	Spherical	6, 9, 13, 15	~5.1 (6 nm)	100	47
		Ta_2O_5	(2-diethylphosphatoethyl)triethoxysilane	Spherical	~6	-	-	48
		TaS_2	1,2-distearoyl-sn-glycero-3-phosphoethanolamine-N-[methoxy(polyethylene glycol)-3000	Nanosheet	50–100	6.3	120	50
W	74	Na_2WO_4	D-glucuronic acid	Spherical	3.2	~10	70	51
		Rb_xWO_3	polyvinyl pyrrolidone	Nanorod	5×20–40	~7.1	70	52
		$WO_{2.9}$	Polyethylene glycol	Nanorod	4.4×13.1	1.9	80	53
		WO_3	poly-caprolactone and Polyethylene glycol	2D platelet	30–100×~5–10	~10	49	54
		$MnWO_4$	Amino acid	Nanorod	20×50	~4.5	120	55
Pt	78	Pt	Bovine serum albumin	Spherical	2.1	16.8	120	56
		Pt	Polyacrylic acid, poly(acrylic acid-co-maleic acid), poly(methyl vinyl ether-alt-maleic acid)	Spherical	2.0	16.4 18.4	50 70	57
		Pt	Mercaptoaminopolyglycol-chlorin e6	Mesophorous	70	3.1	120	58
		Pt	polyethylene glycol	Mesophorous	94	5.5	120	59

Preprints (www.preprints.org) | NOT PEER-REVIEWED | Posted: 23 August 2023 doi:10.20944/preprints202308.1571.v1

		Pt	poly(maleic anhydride-alt-1-octadecene)– Polyethylene glycol	Nanowor m	~3 × ~10	3.9	-	60
		Pt	Extract from Prosopis farcta fruits	Spherical	3.8	6.6	80	61
		Pt	Human serum albumin	Spherical	6.7	~5.6	-	62
		Pt	Polyethylene glycol	Hollow cube	30	~5.39	-	63
Au	7 9	Au	Polyethylene glycol	Spherical	31	5.0	120	64
		Au	Polyethylene glycol	Spherical	10	4.8	50	65
		Au	Mercaptosuccinc acid	Spherical	4.7, 13.2, 35.0, 76.4	10.6 13.0 (no particle size dependen t)	70 45	66
		Au	Bovine serum albumin	Spherical	11.2	~5.6	120	67
		Au	Polyethylene glycol-polyethyleneimine	Spherical	1.9, 2.9, 3.9, 4.6	~9 (2.9 nm)	-	68
		Au	Lactobionic acid	Spherical	2.7	8.5	80	69
		Au	Poly(amidoamine) dendrimer	Spherical	1.9, 2.8, 4.0	9.8 (4.0 nm)	80	70
		Au	G5.NH_2- fluorescein isothiocyanate-(polyethylene glycol- α-tocopheryl succinate)-(polyethylene glycol- folic acid) dendrimer	Spherical	3.3	~6.0	80	71
		Au	Gum Arabic	Spherical	15–20	~4.9	80, 140	72
		Au	Folic acid-conjugated silica	Nanorod	17.8× 46. 0	4.9	-	73
		Au	Glycol chitosan	Spherical	24	~2.8	70	74
		Au	Diatrizoic acid- Aptamer	Spherical	2.4	8.2	-	75
		Au	Gum Arabic	Spherical	1.85	~4.3	80	76
		AuAg (3:1)	Folic acid-5 poly(amidoamine) dendrimer	Spherical	13.4	~6.3	100	77
		Au	Polyethylene glycol	Spherical	3.9, 14.8, 50.6, 78.9, 99.2, 152.3	4.0– 4.2 (nearly particle size	80	78

Preprints (www.preprints.org) | NOT PEER-REVIEWED | Posted: 23 August 2023 doi:10.20944/preprints202308.1571.v1

						independent)		
		Au	cathepsin	Spherical	10, 30, 100	25.4 22.0	35 85	79
		Au	heparin-amino acid 3,4-dihydroxyphenylalanine	Spherical	24.0	21.9	70	80
Bi	83	Bi_2O_3	Polyacrylic acid	Spherical	2.3	11.7	70	32
		BiOI	D-glucuronic acid	Spherical	1.9	~21	70	82
		BiOI	Polyvinyl pyrrolidone	Spherical	2.8	~20	75	83
		Bi_2S_3	Polyvinyl pyrrolidone	Nanosheet	10–50×3–4	~9.7	50	84
		Bi	1,2-propanediol and glucose	Faceted	74	~5.9	80	85
		Bi	poly(DL-lactic-co-glycolic acid)	Spherical	38	10.2	80	86
		Bi	Oligosaccharide	Spherical	22	8.5 6.4	80 120	87
		Bi_2Se_3	Bovine serum albumin	Spherical	2.7	7.06	55	88

[1] Z: atomic number. [2] Size: nanoparticle diameter = d; nanorod = d × ℓ; nanosheet or nanoplate = d × w or d × ℓ × w (d: diameter; ℓ: length; w: thickness).

CT and magnetic resonance imaging (MRI) are the most widely used clinical imaging techniques. Both techniques provide high spatial resolution (~1 mm) and three-dimensional anatomical images with high penetration depths suitable for whole body imaging [90], and they can be used to diagnose various conditions, including tumors, fractures, and internal bleeding. CT offers faster scanning than MRI, but its sensitivity to the imaging probe is less than that of MRI [90], requiring approximately ten times higher injection doses for iodine contrast agents compared with gadolinium contrast agents in MRI. This high injection dose of iodine-based CT contrast agents may be a burden to patients [91] and can be reduced using heavy metal-based NPs owing to their increased imaging sensitivity.

3. Heavy Metal-Based CT Contrast Agents

3.1. Noble Metal-Based NPs

Noble metal-based NPs can exist in pure metallic forms (Pt, Pd, Ag, and Au) or occasionally in chemical forms. They exhibit additional photothermal properties useful for cancer therapy [92].

3.1.1. Pd (Z = 46) NPs (Pd-NPs)

Lyu et al. synthesized cysteamine-coated FePd bimetallic nanodots (d = 3.4 nm) (Figure 2a) as trimodal CT-MRI-photoacoustic imaging agents [24]. They observed an X-ray attenuation efficiency of 2.6 HU/mM, which was higher than that of the commercial iodine contrast agent Iopromide (2.0 HU/mM). In addition, high contrast enhancement was observed in the in vivo CT images of BALB/c mice at the tumor site 12 h after intravenous injection (dose = 50 μL, 10 mgPd/mL) (Figure 2b).

Preprints (www.preprints.org) | NOT PEER-REVIEWED | Posted: 23 August 2023 doi:10.20944/preprints202308.1571.v1

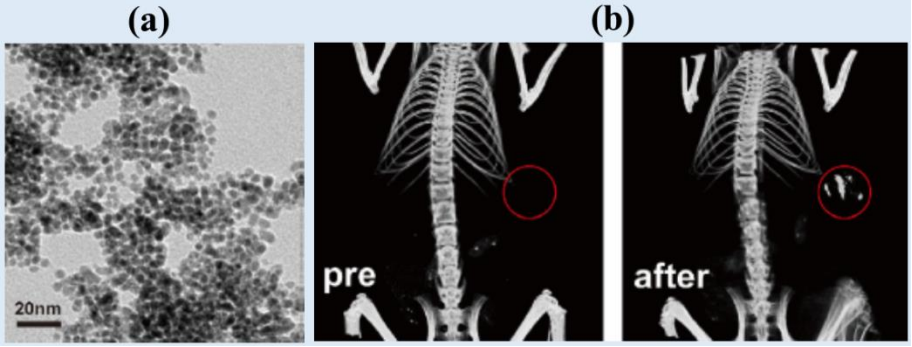

Figure 2. (**a**) TEM image at 20 nm scale. (**b**) In vivo CT images at the tumor site (labeled with red circles) of mice before (labeled as "pre") and 12 h after intravenous injection [24].

3.1.2. Ag (Z = 47) NPs (Ag-NPs)

Liu et al. synthesized dendrimer-stabilized Ag-NPs (Ag-DSNPs) with particle diameter control (d = 8.8, 12.4, 16.1, and 23.2 nm) [25]. Amine-terminated generation 5 poly(amidoamine) dendrimers were used to encapsulate Ag-NPs. The X-ray attenuation efficiency (η) depended on the particle diameter such that η (~7.2 HU/mM; 16.1 nm) > η (~4.6 HU/mM; 12.4 nm) > η (~4.0 HU/mM; 23.2 nm) > η (~2.4 HU/mM; 8.8 nm) at 80 kVp. The η value of the 16.1 nm Ag-NPs was similar to that of the commercial iodine contrast agent Omnipaque. For in vivo CT experiments, Ag-DSNPs (d = 16.1 nm) exhibited contrast enhancements at the injection site (dose = 50 μL, [Ag] = 0.1 M), whereas Omnipaque did not because of its fast diffusion owing to its low molecular weight.

Zhang et al. synthesized spherical and monodispersed hyaluronic acid-coated Ag-NPs (HA–Ag-NPs) (d = ~10 nm, HD = 13.5 nm) (Figure 3a) [26]. The HA-Ag-NPs exhibited excellent long-term stability in water and low cytotoxicity. HA-Ag-NPs demonstrated strong X-ray attenuation in the in vitro phantom images which increased with increasing Ag-concentration (Figures 3b and 3d). The NPs exhibited an X-ray attenuation coefficient of 3.5 HU/mM.

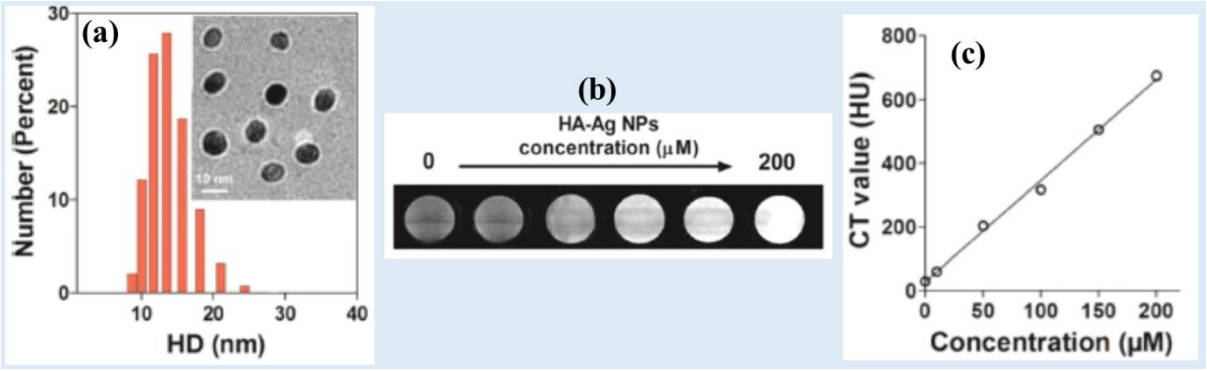

Figure 3. (a) Histogram of the hydrodynamic diameter (HD) distribution of HA-Ag-NPs based on DLS and cryo-TEM (inset). (**b**) Phantom images as a function of Ag-concentration. (**c**) CT values (i.e., X-ray attenuation) of HA-Ag-NPs as a function of Ag-concentration [26].

Hsu et al. synthesized glutathione-conjugated Ag_2S NPs with size control (d = 2.3, 3.1, 4.1, and 5.1 nm) based on the reaction time [27]. Because the NPs were ultrasmall, they were renal-excretable. For example, 85% of the injected 3.1-nm glutathione-conjugated Ag_2S NPs were excreted *via* the renal system as urine. For the synthesized particle diameter range, the X-ray attenuation efficiency was nearly independent of the particle diameter and decreased with increasing X-ray tube voltages such that 80 kVp (~3.5 Hu/mM) > 100 kVp (~2.7 HU/mM) > 120 kVp (~2.3 HU/mM) > 140 kVp (~1.9 HU/mM). In addition, the X-ray attenuation efficiency was lower than that of the commercial iodine contrast agent Iopamidol (~5.1 HU/mM at 80 kVp, ~4.3 HU/mM at 100 kVp, ~3.4 Hu/mM at 120 kVp, and ~3.0 Hu/mM at 140 kVp). The potential of Ag_2S NPs as CT contrast agents was demonstrated in vivo by observing contrast enhancements at the bladder, heart, and kidneys after intravenous injection (dose = 250 mg Ag/kg).

Preprints (www.preprints.org) | NOT PEER-REVIEWED | Posted: 23 August 2023 doi:10.20944/preprints202308.1571.v1

Cui et al. synthesized bovine serum albumin (BSA)-stabilized Ag nanodots (d = 5.8 nm), which exhibited an X-ray attenuation efficiency of 5.7 HU/mM, higher than that of the commercial iodine contrast agent Iopromide (4.3 HU/mM) [28]. The NPs were intratumorally injected (injection dose = 10 mg/mL, 20 μL) and contrast enhancements at the mice tumor site were observed after injection and then decreased with time, demonstrating their potential as a CT contrast agent.

3.1.3. Pt (Z = 78) NPs (Pt-NPs)

Wang et al. developed an albumin-mediated one-pot synthesis method to generate ultrasmall Pt@BSA NPs for CT imaging [56]. The Pt@BSA NPs with a core size of 2.1 nm showed excellent colloidal stability, hemocompatibility, and biocompatibility. The X-ray attenuation efficiency of Pt@BSA NPs (i.e., 16.8 HU/mM) at 120 kVp was approximately 2.4 times higher than that of the commercial iodine contrast agent Ultravist at the same concentration (~6.3 HU/mM). The contrast enhancement of the heart was observed 5 min after the intravenous injection of the Pt@BSA NPs, whereas no contrast enhancement was observed at the heart after the intravenous injection of Ultravist. Therefore, the Pt@BSA NPs showed better CT imaging capabilities than iodine-based CT contrast agents.

Recently, Saidi et al. designed Pt-NPs coated with poly(acrylic acid) (PAA), poly(acrylic acid-co-maleic acid) (PAAMA), or poly(methyl vinyl ether-alt-maleic acid) (PMVEMA) (d = 2.0 nm, Figure 4a), which exhibited high X-ray attenuation efficiencies (*i.e.*, 16.4 HU/mM at 50 kVp and 18.4 HU/mM at 70 kVp) that were approximately four times higher than those of Ultravist at the same atomic concentration (Figures 4b and 4c) [57]. Furthermore, the NPs exhibited approximately 500 times higher X-ray attenuation efficiency at the same density (Figure 4c).

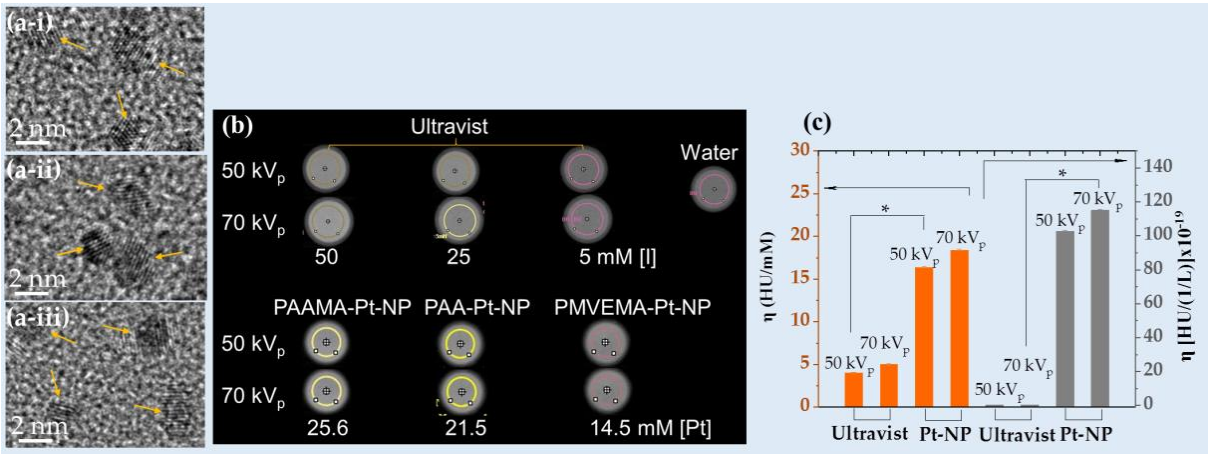

Figure 4. (**a**) TEM images of (i) PAA-, (ii) PAAMA-, and (iii) PMVEMA-coated Pt-NPs at 2 nm scale: arrows indicate NPs. (**b**) Phantom images at 50 and 70 kVp. (**c**) Histogram of X-ray attenuation efficiency. The commercial iodine contrast agent Ultravist was used as a reference [57].

Zhang et al. synthesized Ce6-PEG-coated mesoporous Pt nanoplatforms (Pt@PEG-Ce6) (Ce6 = photosensitizer chlorin e6, d = 70 nm, and pore diameter = 11 nm) [58]. The Pt@PEG-Ce6 exhibited an X-ray attenuation efficiency of 3.1 HU/mM at 120 kVp. In addition, the contrast at the tumor significantly increased after intravenously injecting 100 mL of Pt@PEG-Ce6 (1 mg/mL) into the mice, showing that the NPs can be used as a CT contrast agent.

Fu et al. synthesized mesoporous Pt-NPs (mesoPt-NPs) using Pluronic F127 as a structure-directing agent without seeds or organic reagents [59]. The synthesized mesoPt-NPs had a spherical structure and uniform diameter (94 nm). The surface of the mesoPt-NPs was modified with PEG, and the prepared mesoPt-PEG showed excellent biocompatibility and an X-ray attenuation efficiency of 5.547 HU/mM at 120 kVp.

Ma et al. synthesized poly(maleic anhydride-alt-1-octadecene)–PEG-coated (or simply PEGylated) Pt nanoworms (HD = ~100 nm) [60]. The Pt-PEG nanoworms exhibited an X-ray attenuation efficiency of 3.9 HU/mM. In addition, they observed contrast enhancements at the tumor site after subcutaneous injection (dose = 16 mg/kg).

Preprints (www.preprints.org) | NOT PEER-REVIEWED | Posted: 23 August 2023 doi:10.20944/preprints202308.1571.v1

Jameel et al. synthesized highly stable, biocompatible, and ultrasmall Pt-NPs with a mean diameter of 3.8 nm using a one-step, one-pot, eco-friendly, and simple process [61]. They used an extract from Prosopis farcta fruits as a reducing agent and stabilizer and obtained an X-ray attenuation efficiency of 6.6 HU/mM at 80 kVp, which was higher than that of the commercial iodine contrast agent Omnipaque (3.1 HU/mM).

Tang et al. synthesized human serum albumin (HSA)-coordinated monodisperse 6.7-nm Pt-NPs [62]. The synthesized HSA-coordinated Pt-NPs exhibited an X-ray attenuation efficiency of ~5.6 HU/mM, which was higher than that of Iopromide (~5.2 HU/mM). To evaluate their in vivo CT imaging ability, the HSA-coordinated Pt-NPs were intratumorally injected at 250.0 μmol Pt/kg, and they demonstrated higher contrast enhancements at the tumor site than those obtained with Iopromide.

Wang et al. synthesized hollow Pt cubes (or spirals) with an average size of 30 nm, which have been modified with PEG-SH for biocompatibility [63]. Pt spirals offered higher contrast with an X-ray attenuation efficiency of 5.39 HU/mM than that of Omnipaque (4.76 HU/mM). Their superiority as a CT contrast agent was demonstrated *via* in vivo imaging, as evidenced by the significant contrast enhancement at the tumor site observed 24 h after intravenous injection (a 1.45-fold increase against preinjection).

3.1.4. Au (Z = 79) NPs (Au-NPs)

Among noble metal-based NPs, Au-NPs have been most intensively investigated as CT contrast agents owing to the superior X-ray attenuation ability and biocompatibility of Au [4]. In addition, Au-NPs possess photothermal properties applicable to cancer therapy [92,93].

Dong et al. generated six PEGylated Au-NPs with various particle diameters (4, 15, 50, 79, 100, and 152 nm; HD = 24.1, 40.7, 69.9, 96.9, 104.8, and 140.6 nm, respectively) and found that X-ray attenuation did not depend on the Au-NP size (4.0–4.2 HU/mM at 80 kVp) [78]. They observed that smaller Au-NPs (4 nm and 15 nm) provided CT contrast with a longer circulation time compared to larger Au-NPs because they are more difficult to be removed by mononuclear phagocytic systems as they pass through the liver and kidneys, leading to high accumulation of Au-NPs in the blood. On the other hand, large Au-NPs (>50 nm) were simply deposited in the liver and spleen, providing excellent CT contrast in those areas.

Tsvirkun et al. synthesized Au-NPs with diameters of 10, 30, and 100 nm [79]. The cathepsin-labeled Au-NPs exhibited an X-ray attenuation efficiency of 25.2 HU/mM at 35 kVp and 22.0 HU/mM at 85 kVp, which were slightly higher than those of the iodine contrast agent (5.4 and 4.0 HU/mM, respectively). In addition, they observed that enhanced in vivo CT imaging signals could be achieved at the tumor site using 10- and 30-nm Au-NPs rather than 100-nm Au-NPs owing to more efficient diffusion of smaller NPs after intravenous injection.

Sun et al. synthesized heparin-amino acid 3,4-dihydroxyphenylalanine (DOPA)- conjugated Au-NPs (HEPA-Au-NPs) (d = 24.0 nm; HD = 54.6 nm) and demonstrated low toxicity and sustained stability [80]. They applied HEPA-Au-NPs as a liver-specific CT imaging agent. The average size of the heparin coating layers on the surface was approximately 20 nm, which was almost the size of the bare Au-NPs, as can be observed by TEM (Figure 5a). HEPA-Au-NPs provided 21.9 HU/mM at 70 kVp, whereas the commercial iodine contrast agent eXIA 160 provided 4.2 Hu/mM. In vivo micro-CT images revealed that HEPA-Au-NPs produced enhanced liver-specific CT images compared with iodine-based contrast agents (Figure 5b). This platform showed potential as a molecular imaging probe and liver-specific CT imaging agent for liver cancer.

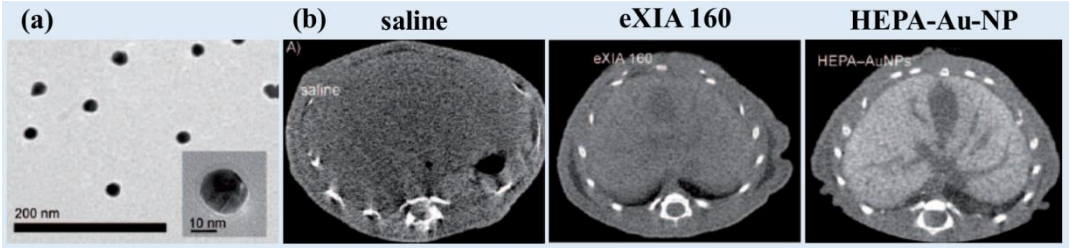

Figure 5. (**a**) TEM image of HEPA–Au-NPs. **(b)** Cross-sectional in vivo micro-CT images of the liver 2 h after the injection of saline, eXIA 160 (800 mg I /kg), and HEPA-Au-NPs (250 mg Au /kg) [80].

Preprints (www.preprints.org) | NOT PEER-REVIEWED | Posted: 23 August 2023 doi:10.20944/preprints202308.1571.v1

Hainfeld et al. used 1.9-nm Au-NPs (Nanoprobes, Inc., preparation # 1101, Yaphank, New York, USA) for in vivo mice experiments [81]. The injection dose was 0.01 mL/g for the Au-NP solution (270 mg Au/mL). After intravenous injection via mice tails, high-resolution CT images of the blood vessels were obtained, whereas they were not obtained with Omnipaque.

3.2. Lanthanide (Ln)-Based NPs

Ln has a higher X-ray attenuation coefficient than iodine (I) [4] and thus, can be used in CT contrast agents. In addition, Ln has optical and magnetic properties, which are useful to develop multimodal imaging agents.

3.2.1. Ce (Z = 58)-Based NPs

Ce-based NPs possess various properties useful for biomedical applications, such as high X-ray attenuation [4] and antioxidant properties [94].

Naha et al. used a precipitation method to synthesize dextran-coated CeO_2 NPs (Dex-Ce-NPs) (d = 4.8 nm and HD = 17.5 nm) (Figure 6a) as CT contrast agents for gastrointestinal tract (GIT) imaging [29]. The Dex-Ce-NPs exhibited an X-ray attenuation efficiency of ~6.3 HU/mM (80 kVp), ~4.8 HU/mM (100 kVp), ~3.8 HU/mM (120 kVp), and ~3.2 HU/mM (140 kVp). The Dex-Ce-NPs exhibited no contrast in the large intestines of healthy mice, whereas they exhibited contrast in the colitis-affected region (Figure 6b). In addition, the Dex-Ce-NPs helped to reduce oxidative damage due to CT scans by scavenging free radicals generated owing to ionizing X-ray radiation.

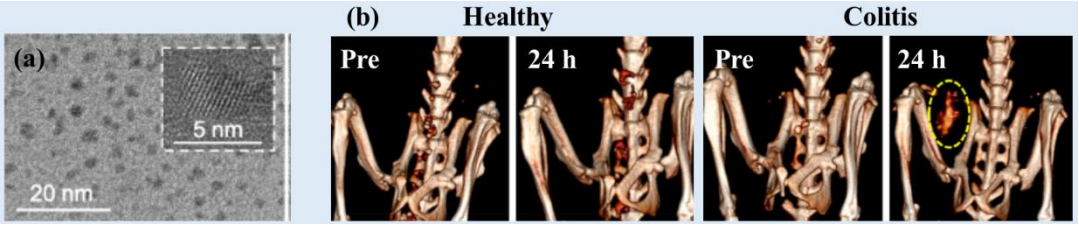

Figure 6. (**a**) TEM images of Dex-Ce-NPs at 20 nm scale (inset: 5 nm scale). (**b**) CT images of healthy (left) and colitis (right) mice obtained before (labeled as "pre") and 24 h after the oral administration of Dex-Ce-NPs. The yellow dashed circle indicates CT contrast due to Dex-Ce-NPs accumulated at the colitis-affected region at 24 h after injection [29].

García et al. synthesized albumin-stabilized 5.1-nm CeO_2 NPs using a chemical precipitation method in a basic aqueous solution [30]. The NPs exhibited contrast enhancements at the liver, whereas the commercial iodine contrast agent Iopamidol-370 exhibited fast accumulation at the kidneys and subsequent renal excretion. In addition, the intratumoral injection of the albumin-stabilized CeO_2 NPs led to contrast enhancements at the tumor for up to 7 days after injection.

3.2.2. Gd (Z = 64)-Based NPs

Ahmad et al. [31] developed iodine compound (*i.e.*, $C_8H_4I_3NO_4$)-coated ultrasmall Gd_2O_3 NPs having a mean diameter of ~2 nm **(**Figure 7a**)**. They observed an X-ray attenuation efficiency of 11.8 HU/mM at 70 kVp. Following intravenous tail injection, brighter contrast enhancements were observed at the mouse bladder (indicated by B in Figure 7b). The contrast at the region-of-interest (ROI) of the bladder, denoted by the small dotted circle in Figure 7b, showed that it peaked at approximately 30 min after injection and then gradually reduced over time (Figure 7c), indicating that the sample solution was expelled through the bladder as urine. As a result, the potential of the Gd_2O_3 NPs as a CT contrast agent was demonstrated.

Preprints (www.preprints.org) | NOT PEER-REVIEWED | Posted: 23 August 2023 doi:10.20944/preprints202308.1571.v1

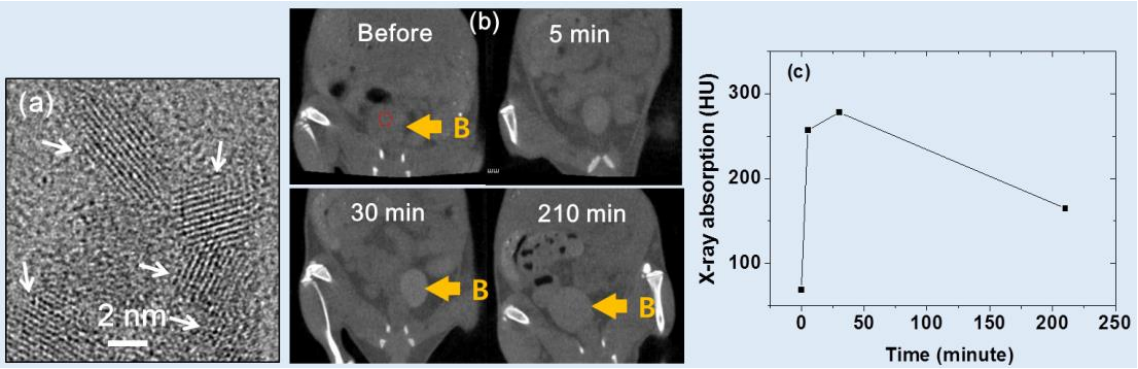

Figure 7. (**a**) HRTEM image of ultrasmall Gd_2O_3 NPs coated with the iodine compound (*i.e.*, $C_8H_4I_3NO_4$) (indicated with arrows). (**b**) In vivo CT images of a mouse bladder (marked B) at 70 kVp. (**c**) X-ray absorption of the ROI at the bladder indicated by the small dotted circle (B) before and after the intravenous injection of an aqueous NP sample into the mouse tail [31].

Ghazanfari et al. examined the X-ray attenuation characteristics of PAA-coated ultrasmall Gd_2O_3 NPs with an average particle diameter of 1.9 nm. The samples showed excellent biocompatibility and good colloidal stability. The PAA-coated Gd_2O_3 NPs demonstrated higher X-ray attenuation (5.9 HU/mM) than Ultravist (4.40 HU/mM) at 70 kVp [32].

Zheng et al. synthesized PAA-capped GdF_3 nanoplates (10.6 × 7.0 × 4.2 nm) as bimodal MRI-CT contrast agents [35]. The nanosheets exhibited ~7.9 HU/mM at 60 kVp, which was higher than that of the commercial iodine contrast agent Iohexol (~4.8 HU/mM).

3.2.3. Dy (Z = 66)-Based NPs

Dy has a high X-ray attenuation coefficient [4]. Therefore, Dy-based NPs can strongly attenuate X-rays, leading to high contrast in CT images.

Recently, Ghazanfari et al. synthesized PAA-coated ultrasmall Dy_2O_3 NPs with an average particle diameter of 1.8 nm and characterized their X-ray attenuation properties [32]. They observed an X-ray attenuation efficiency of 6.1 HU/mM at 70 kVp for the Dy_2O_3 NP suspension, which was greater than that of Ultravist (4.4 HU/mM).

Olifirenko et al. synthesized polyethyleneimine-coated Dy_2O_3 NPs (d = 79–102 nm) in aqueous media and observed an X-ray attenuation efficiency of ~5 HU/mM at 120 kVp [36].

Gómez-Gónzalez et al. synthesized PAA-coated $DyVO_4$ NPs (d = 60 nm and HD = 81 nm) using a polyol method [37]. They observed an X-ray attenuation efficiency of 4.8 HU/mM at 65 kVp, which was higher than 1.6 HU/mM of Iohexol.

3.2.4. Ho (Z = 67)-Based NPs

Zhang et al. synthesized PEG-modified HoF_3 NPs using a one-pot solvothermal technique [38]. The PEG-HoF_3 NPs were uniform in size and exhibited excellent dispersibility in aqueous solution (d = 38 nm and HD = ~100 nm) (Figure 8a). Studies showed that the X-ray attenuation efficiency was 19.0 HU/mM at 120 kVp, which was higher than 3.0 HU/mM for Iohexol. The PEG-HoF_3 NPs demonstrated good biocompatibility and low toxicity according to histological studies and cytotoxicity evaluation. For in vivo CT images, PEG-HoF_3 NP sample solution was injected into Kunming mice tail veins with tumor (dose = 100 μL, 2 mg/mL). The distribution of PEG-HoF_3 NPs was monitored by a CT scanner at different time points. The enhanced brightness of the tumor site and liver was observed up to 24 h after injection compared with that of preinjection (Figure 8b).

Preprints (www.preprints.org) | NOT PEER-REVIEWED | Posted: 23 August 2023 doi:10.20944/preprints202308.1571.v1

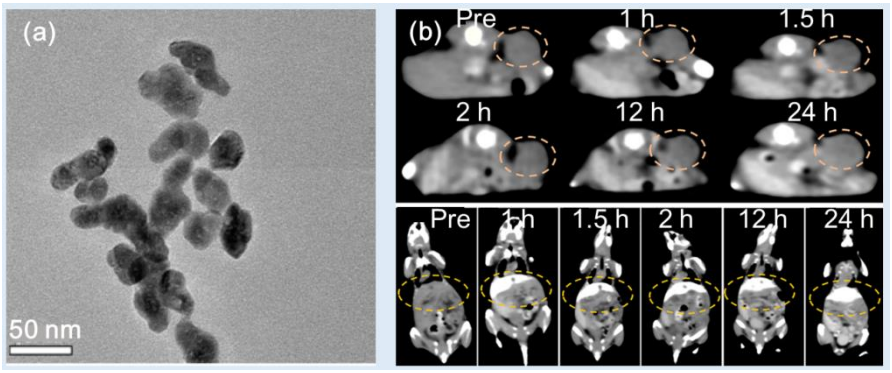

Figure 8. (**a**) TEM image of PEG-HoF_3 NPs at 50 nm scale. (**b**) In vivo CT images of tumor-bearing Kunming mice, showing bright contrast enhancements at the tumor site (top) and liver (bottom) up to 24 h after intravenous tail injection [38]. Dotted circles indicate tumor (top) and liver (bottom).

Ni et al. synthesized PEGylated $NaHoF_4$ NPs with various particle diameters (d = 3.2, 7.4, and 13.2 nm; HD = 12.9, 19.0, 22.7 nm) and nanorods (28.9 × 16.7 nm) by controlling ligand concentration, temperature, and time [40]. They used 3.2-nm PEGylated $NaHoF_4$ NPs to measure an X-ray attenuation efficiency of 6.9 HU/mM at 120 kVp, which was higher than 2.1 HU/mM of the commercial iodine contrast agent Iobitridol. They also observed enhanced contrast at the thigh of Kunming mice after direct injection of 3.2 nm PEGylated $NaHoF_4$ NPs into the thigh.

Gómez-Gónzalez et al. synthesized PAA-coated $HoVO_4$ NPs (d = 65 nm and HD = 74 nm) using a polyol method [37]. They observed an X-ray attenuation efficiency of 4.8 HU/mM at 65 kVp, which was higher than 1.6 HU/mM of Iohexol.

3.2.5. Yb (Z = 70)-Based NPs

Yb has a high X-ray attenuation coefficient [4], making Yb-based NPs promising high-performance CT contrast agents.

The X-ray attenuation properties of PAA-coated ultrasmall Yb_2O_3 NPs with an average particle diameter of 1.7 nm were investigated by Ghazanfari et al. [32]. The X-ray attenuation efficiency of 6.8 HU/mM of the Yb_2O_3 NP suspension was higher than 4.4 HU/mM of Ultravist.

Liu et al. synthesized $Yb(OH)CO_3$ NPs (d = 170 nm) using a one-pot urea-based homogeneous precipitation method (Figure 9b) [44]. To measure CT contrasts, the $Yb(OH)CO_3$ NPs and a commercial iodine contrast agent, Iobitridol, were dispersed in PBS buffer containing 1% agarose with different Yb and I concentrations over the concentration range from 0 to 25 mg/mL. The $Yb(OH)CO_3$ NPs exhibited an X-ray attenuation efficiency of ~9.0 HU/mM at 120 kVp, which was higher than ~3.6 HU/mM of Iobitridol. In in vivo CT studies, the $Yb(OH)CO_3$ NPs (injection dose: 1.0 mL of 50 mg Yb/mL) provided higher CT contrast in the kidneys (top, left) and bladder (bottom, left) than Iobitridol (top and bottom, right) (injection dose: 0.3 mL of 350 mg I/mL) after intravenous injection at 120 kVp (Figure 9b), demonstrating the potential of the $Yb(OH)CO_3$ NPs as a CT contrast agent.

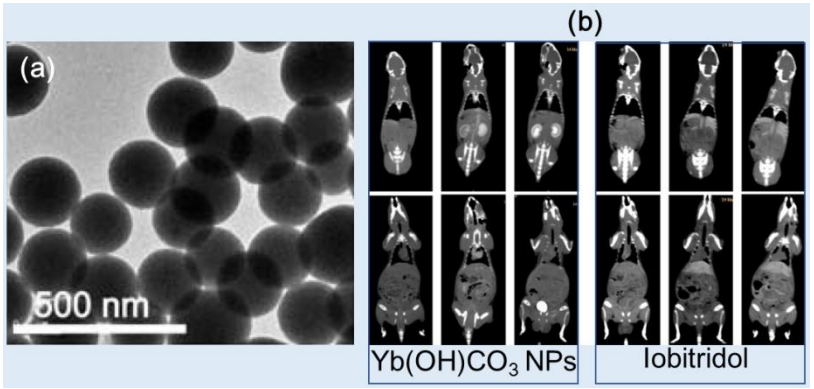

Figure 9. (**a**) TEM images of $Yb(OH)CO_3$ NPs at 500 nm scale. (**b**) In vivo CT images of rats before and after the injection of $Yb(OH)CO_3$ NPs (left) and Iobitridol (right) at 120 kVp [44].

Preprints (www.preprints.org) | NOT PEER-REVIEWED | Posted: 23 August 2023 doi:10.20944/preprints202308.1571.v1

Liu et al. synthesized oleic acid-coated $NaYbF_4$:Er NPs (2.0% Er) (simply OA-UCNPs) (d = 40 nm) and modified OA-UCNPs with phospholipid-polyethylene glycol terminated with carboxylic acid (PL-PEG-COOH) (or simply DSPE-PEG 2000) to obtain PEG-UCNPs for dispersibility in water [45]. The PEG-UCNPs exhibited an X-ray attenuation efficiency of ~9.9 HU/mM at 120 kVp, which was higher than ~3.4 HU/mM of Iobitridol. In addition, the PEG-UCNPs exhibited high contrast in the heart, liver, spleen, and kidneys after intravenous injection at 120 kVp, whereas most of the Iobitridol accumulated in the urinary organs (kidney and bladder), and no contrast was detected in the heart, vessels, or other organs, indicating the short circulation time and rapid vascular permeation of Iobitridol.

Liu et al. synthesized PEGylated Er^{3+}-doped (5 mol%) Yb_2O_3 upconversion NPs (PEG-UCNPs) (d = 170 nm) as high-performance contrast agents [46]. The potential of the PEG-UCNPs in upconversion fluorescence imaging and CT was investigated in vitro and in vivo. The NPs exhibited an X-ray attenuation efficiency of 10.0 HU/mM at 120 kVp, which was higher than 3.0 HU/mM of Iobitridol. In vivo CT studies showed that bright contrast enhancements at the liver were stronger after the intravenous injection of the NP sample compared with those of Iobitridol.

3.3. Other Heavy Metal-Based NPs (Ta, W, and Bi)

Other heavy metal-based NPs such as Ta, W, and Bi have been investigated as CT contrast agents because they possess atomic numbers higher than I, providing more significant X-ray attenuation compared with commercial iodine contrast agents.

3.3.1. Ta (Z = 73)-Based NPs

Ta is a highly biocompatible transition metal with negligible biological side effects in all redox states compared with other transition metals [95]. As a result, Ta has been extensively used in clinical implants, prosthetic joints, stents, and vascular clips for nearly 50 years. Ta has recently been used as a CT contrast agent because of its high X-ray attenuation coefficient [4].

Tantalum oxide (TaOx) NPs of uniform size were synthesized using a simple microemulsion approach by Oh et al. and surface-modified with PEG-silane [47]. The particle diameter could be controlled to obtain 6, 9, 13, and 15 nm by varying the volume of ethanol in the synthesis. The X-ray attenuation efficiency of the TaOx NPs (~5.1 HU/mM at 100 keV) was obtained. The TaOx NPs (840 mg/kg) were injected intravenously into the tail of mice, and contrast enhancements at the liver, heart, kidneys, and spleen were observed shortly after injection.

Bonitatibus et al. synthesized (2-diethylphosphato-ethyl)triethoxysilane-coated Ta_2O_5 NPs (d = ~6 nm and HD = 6 nm) with high stability in water [48]. At equal molar concentrations of tantalum and iodine, the NPs provided greater image contrast than Iopromide across the diagnostic X-ray spectrum between 80 and 140 kVp in in vitro phantom images. In addition, in vivo studies showed high contrast at the arterial system after intravenous injection into mice tails (1 mL of 0.92 M [Ta]) at 120 kVp. The same group improved their performance by synthesizing a zwitterionic siloxane polymer coating, which reduced the viscosity of the concentrated NP solutions by a factor of five, decreased the tissue retention of injected NPs by a factor of ten, and prevented pathological responses in the kidneys [49].

1,2-distearoyl-sn-glycero-3-phosphoethanolamine-N-[methoxy(polyethylene glycol)-3000 (DSPE-PEG)-coated TaS_2 nanosheets (NSs) (or simply PEG-TaS_2 NSs) (d = 50–100 nm and HD = ~110 nm) were synthesized by Liu et al. for safe and efficient cancer treatment (Figure 10a) [50]. The PEG-TaS_2 NSs demonstrated high X-ray attenuation (6.3 HU/mM) at 120 kVp (similar to that of Iobitridol). After intravenous injection (4.5 mg Ta/kg), contrast enhancements at the liver (Figure 10b) were observed, demonstrating the potential of the NSs as a CT contrast agent.

Preprints (www.preprints.org) | NOT PEER-REVIEWED | Posted: 23 August 2023 doi:10.20944/preprints202308.1571.v1

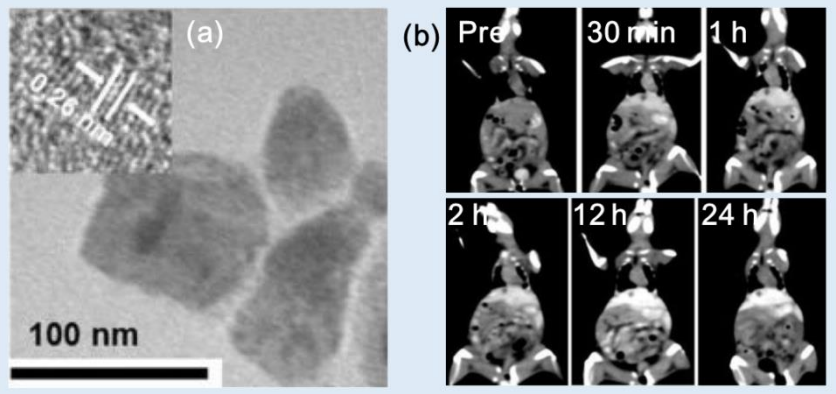

Figure 10. (**a**) TEM image of PEG-TaS_2 NSs (inset is a magnified image showing the lattice fringe). (**b**) Time-dependent whole-body CT imaging of the mouse after the intravenous injection of PEG-TaS_2 NSs at 120 kVp, showing contrast enhancements at the liver [50].

3.3.2. W (Z = 74)-Based NPs

W-based NPs have emerged as promising contrast agents for CT due to their high X-ray attenuation properties [4].

Kim et al. reported D-glucuronic acid-coated Na_2WO_4 NPs as a CT contrast agent [51]. The average particle diameter of the NPs was 3.2 nm (Figure 11a). In vitro phantom images showed stronger X-ray attenuation than that obtained using Ultravist at 70 kVp (Figure 11b): the X-ray attenuation efficiency of the NPs was ~10 HU/mM, which was higher than ~4.5 HU/mM of Ultravist. In addition, in vivo CT images showed contrast enhancements at the kidneys after intravenous injection (0.1 mmol W/kg) at 70 kVp (Figure 11c). Therefore, D-glucuronic acid-coated Na_2WO_4 NPs can be used as a CT contrast agent.

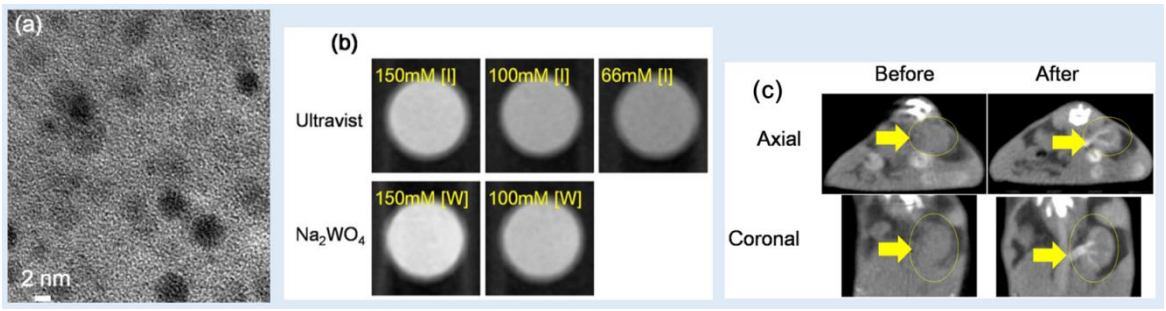

Figure 11. (**a**) HRTEM image of D-glucuronic acid-coated Na_2WO_4 NPs. (**b**) X-ray attenuation phantom images of a solution of D-glucuronic acid-coated Na_2WO_4 NPs at 70 kVp and Ultravist as a function of [I] and [W]. (**c**) Axial and coronal in vivo CT images of a mouse before and after the intravenous injection of D-glucuronic acid-coated Na_2WO_4 NPs into the tail. The arrows and circles identify the kidney [51].

Tian et al. synthesized polyvinyl pyrrolidone (PVP)-coated rubidium tungsten bronze (Rb_xWO_3) nanorods (NRs) (d × ℓ = 5 × 20–40 nm) for CT imaging [52]. The Rb_xWO_3 NRs showed excellent contrast efficacy for CT imaging, as evidenced by an X-ray attenuation efficiency of ~7.1 HU/mM at 70 kVp, which was much larger than that of Ultravist (1.7 HU/mM). The CT signal at the tumor site was immediately apparent after intratumoral injection (3 mg/mL, 20 μL) at 70 kVp, proving that the Rb_xWO_3 NRs can be used as a contrast agent for in vivo CT imaging.

Zhou et al. produced tungsten oxide ($WO_{2.9}$) NRs (length × diameter = 13.1 × 4.4 nm) *via* a facile thermal decomposition method [53]. The NRs were modified with PEG for water solubility and biocompatibility and exhibited better X-ray attenuation efficiency (1.9 HU/mM) compared with that of Iohexol (0.5 HU/mM) at 80 kVp. They used the PEGylated $WO_{2.9}$ NRs for in vivo tumor imaging by intratumorally injecting the sample solution into the nude mice with HeLa tumor (20 mg W/kg). After injection, high contrast enhancements at the tumor site were observed at 60 kVp.

Jakhmola et al. demonstrated WO_3 NPs as a CT contrast agent. A biodegradable polymer poly-caprolactone (PCL) and PEG were used to coat the WO_3 NPs (thickness w = 5–10 nm × d = 30–100 nm

Preprints (www.preprints.org) | NOT PEER-REVIEWED | Posted: 23 August 2023 doi:10.20944/preprints202308.1571.v1

and HD = ~100–200 nm) [54]. Because the PCL layer prevents particle aggregation, the PCL/PEG-coated WO_3 NPs showed good stability in the physiological environment and were nontoxic. The PCL/PEG-coated WO_3 NPs had an X-ray attenuation efficiency of ~15 HU/mM at 49 kVp, which was nearly four times greater than that of the commercial iodine contrast agent Fenestra VC. After the intravenous injection of 0.73 mmol W/kg mice, contrast enhancements were observed at the heart, liver, spleen, and kidneys at 50 kVp and then decayed with time, finally reaching initial contrasts ~10 h after injection.

Dong et al. synthesized biocompatible and high-performance amino acid-capped $MnWO_4$ NRs (d = 20 nm × ℓ = 50 nm) [55]. The NRs exhibited an X-ray attenuation efficiency of 4.5 HU/mM at 120 kVp, which was higher than 3.0 HU/mM of Iobitridol. In in vivo experiments, contrast enhancements at the liver and kidneys were observed after intravenous injection (1 mL of 0.42 M [W]) at 120 kVp.

3.3.3. Bi (Z = 83)-Based NPs

Among nonradioactive elements, Bi has the highest atomic number and thus possesses the highest X-ray attenuation coefficient [4], which is extremely useful as a CT contrast agent. From polonium (Po) (Z = 84) onward, all elements are radioactive and thus are not suitable for biomedical applications.

Ghazanfari et al. synthesized PAA-coated ultrasmall Bi_2O_3 NPs (d = 2.3 nm) (Figure 12a) using a one-pot polyol method, and their X-ray attenuation properties were examined [32]. The X-ray attenuation efficiency of 11.7 HU/mM of the Bi_2O_3 NP suspension at 70 kVp was greater than 4.4 HU/mM of Ultravist. To demonstrate its effectiveness as a CT contrast agent, a sample of the PAA-coated ultrasmall Bi_2O_3 NP suspension was injected into the mouse tail vein (dose = ~0.1 mmol/kg), which is significantly smaller than the average injection dose used for iodine contrast agents (1.5 mmol/kg). CT images were taken before and after the injection, and positive contrasts were observed in the mouse kidney and bladder after injection, as illustrated in Figure 12b. The same group synthesized D-glucuronic acid-coated BiOI NPs [82]. The particle diameter was controlled by varying the solvent volume such that 1.9- and 6.1-nm BiOI NPs were produced using 20 and 10 mL of triethylene glycol, respectively. The D-glucuronic acid-coated BiOI NP (d = 1.9 nm) solution was used to estimate their X-ray attenuation efficiency using in vitro phantom imaging. The sample solution exhibited an exceptionally high X-ray attenuation owing to the combined effects of Bi and I. It exhibited ~21 HU/mM, which was 4.4 times higher than ~4.8 HU/mM of Ultravist and ~127 times stronger at the same number density. These findings highlight the potential of the D-glucuronic acid-coated BiOI NPs as a CT contrast agent.

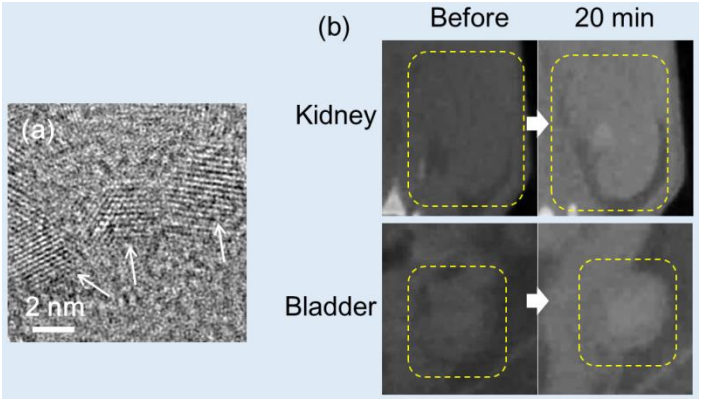

Figure 12. (**a**) HRTEM image of PAA-coated ultrasmall Bi_2O_3 NPs (the arrows indicate NPs). (**b**) In vivo CT images of a mouse kidney and bladder before and 20 min after the intravenous injection of an aqueous NP suspension sample of PAA-coated ultrasmall Bi_2O_3 NPs into the mouse tail (indicated with the dotted squares) [32].

Rabin et al. synthesized bismuth sulfide (Bi_2S_3) nanosheets (NSs) (d × w = 10–50 nm × 3–4 nm) coated with polyvinylpyrrolidone (PVP) [84]. This formulation had a longer in vivo circulation time (140 min), higher stability, and a five fold increase in the X-ray attenuation coefficient of ~9.7 HU/mM than that of Iopromide at 50 kVp. The lymph nodes of mice were clearly visible after intravenous

injection (dose = 11.4 μmol Bi) into Balb/c mice, demonstrating that the Bi_2S_3 NSs could be an excellent CT contrast agent for disease diagnosis.

Swy et al. synthesized 38-nm bismuth(0) NPs encapsulated within 120-nm poly(DL-lactic-co-glycolic acid) (PLGA) NPs using an oil-in-water emulsion methodology [86]. The PLGA-coated Bi NPs in aqueous media exhibited an X-ray attenuation coefficient of 10.2 HU/mM at 80 kVp.

Wei et al. developed oligosaccharide-modified Bi-NPs (OS-Bi-NPs) (d = 22 nm) as a CT contrast agent for GIT imaging [87]. The X-ray attenuation efficiency of the OS-Bi-NPs (*i.e.*, 8.5 HU/mM at 80 kVp and 6.4 HU/mM at 120 kVp) was 1.5 times greater than that of the conventional clinical CT contrast agent $BaSO_4$ used for GIT imaging. In addition, the OS-Bi-NPs were successfully applied in GIT imaging in vivo (dose = 400 μL of 14 mg Bi/mL) at 80 kVp.

Because of chemical stability, dual-based chalcogenides are frequently used as CT contrast agents. Mao et al. obtained 2.7-nm ultrasmall Bi_2Se_3 nanodots stabilized with BSA (BSA-Bi_2Se_3 nanodots), which were synthesized *via* the reaction of hydroxyethylthioselenide with bismuth chloride in aqueous solution under ambient conditions [88]. They found that the X-ray absorption coefficient was approximately 7.06 HU/mM at 55 kVp, higher than that of Iopromide (3.9 HU/mM). The BSA-Bi_2Se_3 nanodots exhibited contrast enhancements at the 4T1 tumor of mice after intratumoral injection (dose = 50 μL, 0.078 mg Bi2Se3) at 55 kVp.

4. Conclusion and Perspectives

Heavy metal-based NPs exhibit comparable or higher X-ray attenuation efficiencies compared with commercial iodine-based counterparts [5–11]. However, side effects such as acute kidney disease may occur because the injection doses (1–2 mmol/kg) of commercial iodine contrast agents are relatively high [13]. This shortcoming may be mitigated using heavy metal-based NPs possessing X-ray attenuation efficiencies higher than those of iodine contrast agents. In this review, the applications of Pd, Ag, Ce, Gd, Dy, Ho, Yb, Ta, W, Pt, Au, and Bi-based NPs as CT contrast agents were discussed, as demonstrated *via* in vitro phantom and in vivo CT images.

Heavy metals can strongly attenuate X-rays because X-ray attenuation is proportional to atomic number (Z) [4]. This makes them advantageous over molecular iodine contrast agents, which possess only three iodines per molecule. In addition, they exhibit longer blood circulation times and consequently, longer imaging times compared with iodine contrast agents. Furthermore, they can be easily surface-functionalized with cancer-targeting ligands, drugs, and other imaging agents, making them suitable for advanced applications [15,16]. Heavy metal-based NPs also possess extremely useful magnetic, optical, and therapeutic properties. Therefore, they can be used as multimodal imaging or theranostic agents.

Although the development of heavy metal-based NPs as CT contrast agents has shown remarkable progress, challenges remain to be addressed. The toxicity of the NPs is one of the major problems. Although numerous studies have shown very low NP toxicity *via* in vitro cellular assays and in vivo histology assays, more research is needed to fully understand their long-term effects and potential side effects due to their accumulation in tissues and organs. One effective approach to solve this toxicity problem is to make NPs completely excretable *via* the renal system as urine after injection within a few hours. To this end, the core and hydrodynamic diameters of NPs must be smaller than ~3 nm [18,19]. In addition, their colloidal stability must be improved because precipitated NPs due to aggregation weakly contribute to X-ray attenuation compared with well-dispersed NPs. In addition, aggregated NPs accumulate in tissues and organs, causing toxicity. Therefore, continuous research on the development of synthetic strategies must be performed to address the long-term toxicity and renal excretion of NPs for in vivo applications.

Author Contributions: Conceptualization, M.Y.A., S.L., T.T., A.K.A.A.S., D.Z., Y.L., G.H.L., S.-W.N., and Y.C.; investigation, M.Y.A., S.L., T.T., G.H.L., S.-W.N., and Y.C.; writing—original draft preparation, M.Y.A.; writing—review and editing, G.H.L. and Y.C.; funding acquisition, G.H.L., Y.C., and S.-W.N. All authors have read and agreed to the published version of the manuscript.

Funding: This work was supported by the Basic Science Research Program of the National Research Foundation (NRF) funded by the Korean government (Ministry of Science, and Information and Communications Technology: MSIT) (Basic Research Laboratory, No. 2021R1A4A1029433).

Institutional Review Board Statement: Not applicable.

Informed Consent Statement: Not applicable.

Data Availability Statement: Not applicable.

Conflicts of Interest: The authors declare no conflict of interest.

References

1. Joudeh, N.; Linke, D. Nanoparticle classification, physicochemical properties, characterization, and applications: a comprehensive review for biologists. *J. Nanobiotechnol.* **2022**, *20*, 262.
2. Kumar, A.; Choudhary, A.; Kaur, H.; Mehta, S.; Husen, A. Metal-based nanoparticles, sensors, and their multifaceted application in food packing. *J. Nanobiotechnol*. **2021**, *19*, 256.
3. Yaqoob, S.B.; Adnan, R.; Khan, R.M.R.; Rashid, M. Gold, silver, and palladium nanoparticles: a chemical tool for biomedical applications. *Front. Chem*. **2020**, *8*, 376.
4. Hubbell, J.H.; Seltzer, S.M. *Tables of X-Ray Mass Attenuation Coefficients and Mass Energy-Absorption Coefficients from 1 keV to 20 MeV for Elements Z = 1 to 92 and 48 Additional Substances of Dosimetric Interest*; NIST: Gaithersburg, MD, USA, 1996. Available online: http://www.nist.gov/pml/data/xraycoef.
5. Yu, S.-B.; Watson, A.D. Metal-based X-ray contrast media. *Chem. Rev.* **1999**, *99*, 2353–2377.
6. Lee, N.; Choi, S.H.; Hyeon, T. Nano-sized CT contrast agents. *Adv. Mater.* **2013**, *25*, 2641–2660.
7. Lusic, H.; Grinstaff, M.W. X-ray-computed tomography contrast agents. *Chem. Rev.* **2013**, *113*, 1641–1666.
8. Liu, Y.; Ai, K.; Lu, L. Nanoparticulate X-ray computed tomography contrast agents: From design validation to in vivo applications. *Acc. Chem. Res.* **2012**, *45*, 1817–1827.
9. Cormode, D.P.; Naha, P.C.; Fayad, Z.A. Nanoparticle contrast agents for computed tomography: A focus on micelles. *Contrast Media Mol. Imaging* **2014**, *9*, 37–52.
10. De La Vega, J.C.; Hafeli, U.O. Utilization of nanoparticles as X-ray contrast agents for diagnostic imaging applications. *Contrast. Media Mol. I* **2015**, *10*, 81–95.
11. Aslan, N.; Ceylan, B.; Koç, M.M.; Findik, F. Metallic Nanoparticles as X-Ray Computed Tomography (CT) Contrast Agents: A Review. *J. Mol. Struct.* **2020**, *1219*, 128599.
12. Spampinato, M.V.; Abid, A.; Matheus, M.G. Current radiographic iodinated contrast agents. *Magn. Reson. Imaging Clin. N. Am*. **2017**, *25*, 697–704.
13. Singh, J.; Daftary, A. Iodinated Contrast Media and Their Adverse Reactions. *J. Nucl. Med. Technol.* **2008**, *36*, 69–74.
14. Taghavi, H.; Bakhshandeh, M.; Montazerabadi, A.; Nazari Moghadam, H.; Mazloom Shahri, S.B.; Keshtkar, M. Comparison of Gold Nanoparticles and Iodinated Contrast Media in Radiation Dose Reduction and Contrast Enhancement in Computed Tomography. *Iran. J. Radiol.* **2020**, *17*, e92446.
15. Swain, S.; Sahu, P.K.; Beg, S.; Babu, S.M. Nanoparticles for cancer targeting: current and future directions. *Curr. Drug. Deliv*. **2016**, *13*, 1290–1302.
16. Wang, M.; Thanou, M. Targeting nanoparticles to cancer. *Pharmacol. Res*. **2010**, *62*, 90–99.
17. Yoshioka, Y.; Higashisaka, K.; Tsutsumi, Y. *Biocompatibility of Nanomaterials*. In: Lu, Z. -R.; Sakuma, S. (eds) *Nanomaterials in Pharmacology. Methods in Pharmacology and Toxicology*. Humana Press, New York, USA, pp. 185–199, **2016**.
18. Choi, H.S.; Liu, W.; Misra, P.; Tanaka, E.; Zimmer, J.P.; Ipe, B.I.; Bawendi, M.G.; Frangioni, J.V. Renal clearance of nano-particles. *Nat. Biotechnol.* **2007**, *25*, 1165–1170.
19. Longmire, M.; Choyke, P.L.; Kobayashi, H. Clearance properties of nano-sized particles and molecules as imaging agents: Considerations and caveats. *Nanomedicine* **2008**, *3*, 703–717.
20. Yoo, J.-W.; Chambers, E.; Mitragotri, S. Factors that control the circulation time of nanoparticles in blood: challenges, solutions and future prospects. *Curr. Pharm. Des*. **2010**, *16*, 2298–2307.
21. Suk, J.S.; Xu, Q.; Kim, N.; Hanes, J.; Ensign, L.M. PEGylation as a strategy for improving nanoparticle-based drug and gene delivery. *Adv. Drug. Deliv. Rev*. **2016**, *99*, 28–51.
22. Jokerst, J.V.; Lobovkina, T.; Zare, R.N.; Gambhir, S.S. Nanoparticle PEGylation for imaging and therapy. *Nanomedicine* **2011**, *6*, 715–728.
23. Mitra, S.; Chakraborty, A.J.; Tareq, A.M.; Emran, T.B.; Nainu, F.; Khusro, A.; Idris, A.M.; Khandaker, M.U.; Osman, H.; Alhumaydhi, F.A.; Simal-Ganara, J. Impact of heavy metals on the environment and human health: novel therapeutic insights to counter the toxicity. *J. King Saud Univ. Sci*. **2022**, *34*, 101865.
24. Lyu, M.; Zhu, D.; Duo, Y.; Li, Y.; Quan, H. Bimetallic Nanodots for Tri-Modal CT/MRI/PA Imaging and Hypoxia-Resistant Thermoradiotherapy in the NIR-II Biological Windows. *Biomaterials* **2020**, *233*, 119656.
25. Liu, H.; Wang, H.; Guo, R.; Cao, X.; Zhao, J.; Luo, Y.; Shen, M.; Zhang, G.; Shi, X. Size-controlled synthesis of dendrimer-stabilized silver nanoparticles for X-ray computed tomography imaging applications. *Polym. Chem.* **2010**, *1*, 1677–1683.
26. Zhang, X.; Yao, M.; Chen, M.; Li, L.; Dong, C.; Hou, Y.; Zhao, H.; Jia, B.; Wang, F. Hyaluronic Acid-Coated Silver Nanoparticles as a Nanoplatform for in Vivo Imaging Applications. *ACS Appl. Mater. Interfaces* **2016**, *8*, 25650–25653.

27. Hsu, J.C.; Cruz, E.D.; Lau, K.C.; Bouché, M.; Kim, J.; Maidment, A.D.A.; Cormode, D.P. Renally Excretable and Size-Tunable Silver Sulfide Nanoparticles for Dual-Energy Mammography or Computed Tomography. *Chem. Mater.* **2019**, *31*, 7845– 7854.
28. Cui, Y.; Yang, J.; Zhou, Q.; Liang, P.; Wang, Y.; Gao, X.; Wang, Y. Renal Clearable Ag Nanodots for in vivo Computer Tomography Imaging and Photothermal Therapy. *ACS Appl. Mater. Interfaces* **2017**, *9*, 5900– 5906.
29. Naha, P.C.; Hsu, J.C.; Kim, J.; Shah, S.; Bouché, M.; Si-Mohamed, S.; Rosario-Berrios, D.N.; Douek, P.; Hajfathalian, M.; Yasini, P.; Singh, S.; Rosem, M.A.; Morgan, M.A.; Cormode, D.P. Dextran-Coated Cerium Oxide Nanoparticles: A Computed Tomography Contrast Agent for Imaging the Gastrointestinal Tract and Inflammatory Bowel Disease. *ACS Nano* **2020**, *14*, 10187–10197.
30. García, A.; Cámara, J.A.; Boullosa, A.M.; Gustà, M.F.; Mondragón, L.; Schwartz, S., Jr.; Casals, E.; Abasolo, I.; Bastús, N.G.; Puntes, V. Nanoceria as Safe Contrast Agents for X-ray CT Imaging. *Nanomaterials* **2023**, *13*, 2208.
31. Ahmad, M.W.; Xu, W.; Kim, S.J.; Baeck, J.S.; Chang, Y.; Bae, J.E.; Chae, K.S.; Park, J.A.; Kim, T.J.; Lee, G.H. Potential dual imaging nanoparticle: Gd_2O_3 nanoparticle. *Sci. Rep.* **2015**, *5*, 8549.
32. Ghazanfari, A.; Marasini, S.; Miao, X.; Park, J.A.; Jung, K.-H.; Ahmad, M.Y.; Yue, H.; Ho, S.L.; Liu, S.; Jang, Y.J.; Chae, K.S.; Chang, Y.; Lee, G.H. Synthesis, characterization, and X-ray attenuation properties of polyacrylic acid-coated ultrasmall heavy metal oxide (Bi_2O_3, Yb_2O_3, $NaTaO_3$, Dy_2O_3, and Gd_2O_3) nanoparticles as potential CT contrast agents. *Colloids Surfaces A Physicochem. Eng. Asp.* **2019**, *576*, 73–81.
33. Lee, E.J.; Heo, W.C.; Park, J.W.; Chang, Y.; Bae, J.-E.; Chae, K.S.; Kim, T.J.; Park, J.A.; Lee, G.H. D-Glucuronic Acid Coated $Gd(IO_3)_3{\cdot}2H_2O$ Nanomaterial as a Potential T_1 MRI-CT Dual Contrast Agent. *Eur. J. Inorg. Chem.* **2013**, *2013*, 2858–2866.
34. Dong, L.; Zhang, P.; Lei, P.; Song, S.; Xu, X.; Du, K.; Feng, J.; Zhang, H. PEGylated GdF_3:Fe Nanoparticles as Multimodal T_1/T_2-Weighted MRI and X-ray CT Imaging Contrast Agents. *ACS Appl. Mater. Interfaces* **2017**, *9*, 20426–20434.
35. Zheng, X.Y.; Sun, L.D.; Zheng, T.; Dong, H.; Li, Y.; Wang, Y.F.; Yan, C.H. PAA-capped GdF_3 Nanoplates as Dual-mode MRI and CT Contrast Agents. *Sci. Bull.* **2015**, *60*, 1092–1100.
36. Olifirenko, V.; Abduraimova, A.; Kang, M.S.; Raja, I.S.; Duisenbayeva, B.; Molkenova, A.; Khamkhash, L.; Hwang, Y.-H.; Han, D.-W.; Atabaev, T.S. Potential applicability of polyethyleneimine PEI-coated Eu_2O_3 and Dy_2O_3 nanoparticles for contrast enhancement in computed tomography. *Nano Express* **2021**, *2*, 010022.
37. Gómez-Gónzalez, E.; Núñez, N.O.; Caro, C.; García-Martín, M.L.; Fernández-Afonso, Y.; de la Fuente, J.M.; Balcerzyk, M.; Ocaña, M. Dysprosium and holmium vanadate nanoprobes as high-performance contrast agents for high-field magnetic resonance and computed tomography imaging. *Inorg. Chem.* **2021**, *60*, 152–160.
38. Zhang, T.; Deng, M.; Zhang, L.; Liu, Z.; Liu, Y.; Song, S.; Gong, T.; Yuan, Q. Facile Synthesis of Holmium-Based Nanoparticles as a CT and MRI Dual-Modal Imaging for Cancer Diagnosis. *Front. Oncol.* **2021**, *11*, 741383.
39. Wang, J.; Ni, D.L.; Bu, W.B.; Zhou, Q.; Fan, W.P.; Wu, Y.; Liu, Y.Y.; Yin, L.K.; Cui, Z.W.; Zhang, X.X.; Zhang, H.; Yao, Z.W. $BaHoF_5$ nanoprobes as high-performance contrast agents for multi-modal CT imaging of ischemic stroke. *Biomaterials* **2015**, *71*, 110–118.
40. Ni, D.; Zhang, J.; Bu, W.; Zhang, C.; Yao, Z.; Xing, H.; Wang, J.; Duan, F.; Liu, Y.; Fan, W.; Feng, X.; Shi, J. PEGylated $NaHoF_4$ nanoparticles as contrast agents for both X-ray computed tomography and ultra-high field magnetic resonance imaging. *Biomaterials* **2016**, *76*, 218–225.
41. Ghazanfari, A.; Marasini, S.; Tegafaw. T.; Ho, S.L.; Miao, X.; Ahmad, M.Y.; Yue, H.; Lee, G.H.; Park, J.A.; Jung, K.-H.; Chang, Y.; Oh, I.T.; Chae, K.-S. X-ray attenuation properties of ultrasmall Yb_2O_3 nanoparticles as a high-performance CT contrast agent. *J. Korean Phys Soc.* **2019**, *74*, 286–291.
42. Silva, M.O.; Kirkwood, N.; Mulvaney, P.; Ellis, A.V.; Stok, K.S. Evaluation of a lanthanide nanoparticle-based contrast agent for microcomputed tomography of porous channels in subchondral bone. *J. Orthopaed. Res.* **2023**, *41*, 447–458.
43. Dong, Y.C.; Kumar, A.; Rosario-Berríos, D.N.; Si-Mohamed, S.; Hsu, J.C.; Nieves, L.M.; Douek, P.; Noël, P.B.; Cormode, D.P. Ytterbium Nanoparticle Contrast Agents for Conventional and Spectral Photon-Counting CT and Their Applications for Hydrogel Imaging. *ACS Appl. Mater. Interfaces* **2022**, *14*, 39274–39284.
44. Liu, J.; Xin, R.; Li, Z.; Golamaully, R.; Zhang, Y.; Zhang, J.; Yuan, Q.; Liu, X. Large-scale and facile synthesis of biocompatible Yb-based nanoparticles as a contrast agent for in vivo X-ray computed tomography imaging. *Curr. Top. Med. Chem.* **2013**, *13*, 513–518.
45. Liu, Y.; Ai, K.; Liu, J.; Yuan, Q.; He, Y.; Lu L. A high-performance ytterbium-based nanoparticulate contrast agent for in vivo X-ray computed tomography imaging. *Angew. Chem.* **2012**, *124*, 1466–1471.
46. Liu, Z.; Li, Z.; Liu, J.; Gu, S.; Yuan, Q.; Ren, J, Qu, X. Long-circulating Er^{3+}-doped Yb_2O_3 up-conversion nanoparticles as an in vivo X-ray CT imaging contrast agent. *Biomaterials* **2012**, *33*, 6748–6757.

47. Oh, M.H.; Lee, N.; Kim, H.; Park, S.P.; Piao, Y.; Lee, J.; Jun, S.W.; Moon, W.K.; Choi, S.H.; Hyeon, T. Large-scale synthesis of bioinert tantalum oxide nanoparticles for X-ray computed tomography imaging and bimodal image-guided sentinel lymph node mapping. *J. Am. Chem. Soc.* **2021**, *133*, 5508–5515.
48. Bonitatibus, P.J.; Torres, A.S.; Goddard, G.D.; FitzGerald, P.F.; Kulkarni, A.M. Synthesis, characterization, and computed tomography imaging of a tantalum oxide nanoparticle imaging agent. *Chem. Comm.* **2010**, *46*, 8956–8958.
49. Bonitatibus, P.J.; Torres, A.S.; Kandapallil, B.; Lee, B.D.; Goddard, G.D.; Colborn, R.E.; Marino, M.E. Preclinical assessment of a zwitterionic tantalum oxide nanoparticle X-ray contrast agent. *ACS Nano* **2012**, *6*, 6650–6658.
50. Liu, Y.; Ji, X.; Liu, J.; Tong, W. W. L.; Askhativa, D.; Shi, J. Tantalum sulfide nanosheets as a theranostic nanoplatform for computed tomography imaging-guided combinatorial chemo-photothermal therapy. *Adv. Funct. Mater*. **2017**, *27*, 1703261.
51. Kim, S.J.; Xu, W.; Ahmad, M.W.; Baeck, J.S.; Chang, Y.; Bae, J.E.; Chae, K.S.; Kim, T.J.; Park, J.A.; Lee, G.H. Synthesis of nanoparticle CT contrast agents: In vitro and in vivo studies. *Sci. Technol. Adv. Mater.* **2015**, *16*, 055003.
52. Tian, G.; Zhang, X.; Zheng, X.; Yin, W.; Ruan, L.; Liu, X.; Zhou, L.; Yan, L.; Li, S.; Gu, Z.; Zhao, Y. Multifunctional Rb_xWO_3 nanorods for simultaneous combined chemo-photothermal therapy and photoacoustic/CT imaging. *Small* **2014**, *10*, 4160–4170.
53. Zhou, Z.; Kong, B.; Yu, C.; Shi, X.; Wang, M.; Liu, W.; Sun, Y.; Zhang, Y.; Yang, H.; Yang, S. Tungsten oxide nanorods: an efficient nanoplatform for tumor CT imaging and photothermal therapy. *Sci. Rep*. **2014**, *4*, 3653.
54. Jakhmola, A.; Anton, N.; Anton.; Messaddeq, N.; Hallouard, F.; Klymchenko, A.; Mely, Y.; Vandamme, T.F. Poly-ε-caprolactone tungsten oxide nanoparticles as a contrast agent for X-ray computed tomography. *Biomaterials* **2014**, *35*, 2981–2986.
55. Dong, K. Liu, Z.; Liu, J.; Huang, S.; Li, Z.; Yuan, Q.; Ren, J.; Qu, X. Biocompatible and high-performance amino acids-capped $MnWO_4$ nanocasting as a novel non-anthanide contrast agent for X-ray computed tomography and T_1-weighted magnetic resonance imaging. *Nanoscale* **2014**, *6*, 2211–2217.
56. Wang, Z.; Chen, L.; Huang, C.; Huang, Y.; Jia, N. Albumin-mediated platinum nanocrystals for in vivo enhanced computed tomography imaging. *J. Mater. Chem. B* **2017**, *5*, 3498–3510.
57. Saidi, A.K.A.A.; Ghazanfari, A.; Liu, S.; Tegafaw, T.; Ahmad, M.Y.; Zhao, D.; Liu, Y.; Yang, S.H.; Hwang, D.W.; Yang, J.-u.; Park, J.A.; Jung, J.C.; Nam, S.-W.; Chang, Y.; Lee, G.H. Facile Synthesis and X-ray Attenuation Properties of Ultrasmall Platinum Nanoparticles Grafted with Three Types of Hydrophilic Polymers. *Nanomaterials* **2023**, *13*, 806.
58. Zhang, L.; Li, M.; Zhou, Q.; Dang, M.; Tang, Y.; Wang, S.; Fu, J.; Teng, Z.; Lu, G. Computed tomography and photoacoustic imaging guided photodynamic therapy against breast cancer based on mesoporous platinum with in situ oxygen generation ability. *Acta Pharm. Sin. B.* **2020**, *10*, 1719–1729.
59. Fu, B.; Dang, M.; Tao, J.; Li, Y.; Tang, Y. Mesoporous platinum nanoparticle-based nanoplatforms for combined chemo-photothermal breast cancer therapy. *J. Colloid Interface Sci.* **2020**, *570*, 197–204.
60. Ma, Q.; Cheng, L.; Gong, F.; Dong, Z.; Liang, C.; Wang, M.; Feng, L.; Li, Y.; Liu, Z.; Li, C.; He, L. Platinum nanoworms for imaging-guided combined cancer therapy in the second near-infrared window. *J. Mater. Chem. B* **2018**, *6*, 5069–5079.
61. Jameel, M.S.; Aziz, A.A.; Dheyab, M.A.; Mehrdel, B.; Khaniabadi, P.M.; Khaniabadi, B.M. Green sonochemical synthesis platinum nanoparticles as a novel contrast agent for computed tomography. *Mater. Today Commun.* **2021**, *27*, 102480.
62. Tang, Y.; Yang, T.; Wang, Q.; Lv, X.; Song, X.; Ke, H.; Guo, Z.; Huang, X.; Hu, J.; Li, Z.; Yang, P.; Yang, X.; Chen, H. Albumin-coordinated assembly of clearable platinum nanodots for photo-induced cancer theranostics. *Biomaterials* **2018**, *154*, 248–260.
63. Wang, Q.; Wang, H.; Yang, Y.; Jin, L.; Liu, Y.; Wang, Y.; Yan, X.; Xu, J.; Gao, R.; Lei, P.; Zhu, J.; Wang, Y.; Song, S.; Zhang, H. Plasmonic Pt Superstructures with Boosted Near-Infrared Absorption and Photothermal Conversion Efficiency in the Second Biowindow for Cancer Therapy. *Adv. Mater*. **2019**, *31*, 1904836.
64. Kim, D.; Park, S.; Lee, J.H.; Jeong, Y.Y.; Jon, S. Antibiofouling polymer-coated gold nanoparticles as a contrast agent for in vivo X-ray computed tomography imaging. *J. Am. Chem. Soc.* **2007**, *129*, 7661–7665.
65. Cai, Q.-Y.; Kim, S.H.; Choi, K.S.; Kim, S.Y.; Byun, S.J.; Kim, K.W.; Park, S.H.; Juhng, S.K.; Yoon, K.-H. Colloidal gold nanoparticles as a blood-pool contrast agent for X-ray computed tomography in mice. *Investig. Radiol.* **2007**, *42*, 797–806.
66. Ross, R.D.; Cole, L.E.; Tilley, J.M.R.; Roeder, R.K. Effects of Functionalized Gold Nanoparticle Size on X-Ray Attenuation and Substrate Binding Affinity. *Chem. Mater.* **2014**, *26*, 1187–1194.
67. Wang, Z.; Chen, L.; Chu, Z.; Huang, C.; Huang, Y.; Jia, N. Gemcitabine-loaded gold nanospheres mediated by albumin for enhanced anti-tumor activity combining with CT imaging. *Mater. Sci. Eng. C* **2018**, *89*, 106–118.

68. Zhou, B.; Zheng, L.; Peng, C.; Li, D.; Li, J.; Wen, S.; Shen, M.; Zhang, G.; Shi, X. Synthesis and Characterization of PEGylated Polyethylenimine-Entrapped Gold Nanoparticles for Blood Pool and Tumor CT Imaging. *ACS Appl. Mater. Interfaces* **2014**, *6*, 17190–17199.
69. Liu, H.; Wang, H.; Xu, Y.; Guo, R.; Wen, S.; Huang, Y.; Liu, W.; Shen, M.; Zhao, J.; Zhang, G.; Shi, X. Lactobionic Acid-Modified Dendrimer-Entrapped Gold Nanoparticles for Targeted Computed Tomography Imaging of Human Hepatocellular Carcinoma. *ACS Appl. Mater. Interfaces* **2014**, *6*, 6944–6953.
70. Guo, R.; Wang, H.; Peng, C.; Shen, M.; Pan, M.; Cao, X.;Zhang, G.; Shi, X. X-ray Attenuation Property of Dendrimer-Entrapped Gold Nanoparticles. *J. Phys. Chem. C* **2010**,114, 50–56.
71. Zhu, J.; Zheng, L.; Wen, S.; Tang, Y.; Shen, M.; Zhang, G.; Shi, X. Targeted cancer theranostics using alpha-tocopheryl succinate-conjugated multifunctional dendrimer-entrapped gold nanoparticles. *Biomaterials* **2014**, *35*, 7635–7646.
72. Kattumuri, V.; Katti, K.; Bhaskaran, S.; Boote, E.J.; Casteel, S.W.; Fent, G.M.; Robertson, D.J.; Chandrasekhar, M.; Kannan, R.; Katti, K.V. Gum arabic as a phytochemical construct for the stabilization of gold nanoparticles: In vivo pharmacokinetics and X-ray-contrast-imaging studies. *Small* **2007**, *3*, 333–341.
73. Huang, P.; Bao, L.; Zhang, C.L.; Lin, J.; Luo, T.; Yang, D.P.; He, M.; Li, Z.M.; Gao, G.; Gao, B.; Fu, S.; Cui, D.X. Folic Acid-conjugated Silica-modified Gold Nanorods for X-ray/CT Imaging-guided Dual-mode Radiation and Photo-thermal Therapy. *Biomaterials* **2011**, *32*, 9796–9809.
74. Sun, I.-C.; Na, J.H.; Jeong, S.Y.; Kim, D.-E.; Kwon, I.C.; Choi, K.; Ahn, C.-H.; Kim, K. Biocompatible Glycol Chitosan-Coated Gold Nanoparticles for Tumor-Targeting CT Imaging. *Pharm. Res.* **2014**, *31*, 1418–1425.
75. Li, C.-H.; Kuo, T.-R.; Su, H.-J.; Lai, W.-Y.; Yang, P.-C.; Chen, J.-S.; Wang, D.-Y.; Wu, Y.-C.; Chen, C.-C. Fluorescence-guided probes of aptamer-targeted gold nanoparticles with computed tomography imaging accesses for in vivo tumor resection. *Sci. Rep.* **2015**, *5*, 15675.
76. Mzwd, E.; Ahmed, N.M.; Suradi, N.; Alsaee, S.K.; Altowyan, A.S.; Almessiere, M.A.; Omar, A.F. Green synthesis of gold nanoparticles in Gum Arabic using pulsed laser ablation for CT imaging. *Sci. Rep.* **2022**, *12*, 10549.
77. Liu, H.; Shen, M.; Zhao, J.; Zhu, J.; Xiao, T.; Cao, X.; Zhang, G.; Shi, X. Facile formation of folic acid-modified dendrimer-stabilized gold–silver alloy nanoparticles for potential cellular computed tomography imaging applications. *Analyst* **2013**, *138*, 1979–1987.
78. Dong, Y.C.; Hajfathalian, M.; Maidment, P.S.N.; Hsu, J.C.; Naha. P.C.; Si-Mohamed, S.; Breuilly, M.; Kim, J.; Chhour, P.; Douek, P.; Litt, H.I.; Cormode, D.P. Effect of Gold Nanoparticle Size on Their Properties as Contrast Agents for Computed Tomography. *Sci. Rep.* **2019**, *9*, 14912.
79. Tsvirkun, D.; Ben-Nun, Y.; Merquiol, E.; Zlotver, I.; Meir, K.; Weiss-Sadan, T.; Matok, I.; Popovtzer, R.; Blum, G. CT Imaging of Enzymatic Activity in Cancer Using Covalent Probes Reveal a Size-Dependent Pattern. *J. Am. Chem. Soc.* **2018**, *140*, 12010–12020.
80. Sun, I.-C.; Eun, D.-K.; Na, J. H.; Lee, S.; Kim, I.-J.; Youn, I.-C.; Ko, C.-Y.; Kim, H.-S.; Lim, D.; Choi, K.; Messersmith, P.B.; Park, T.G.; Kim, S.Y.; Kwom, I.C.; Kim, K.; Ahn, C.-H. Heparin-Coated Gold Nanoparticles for Liver-Specific CT Imaging. *Chem. Eur. J.* **2009**, *15*, 13341–13347.
81. Hainfeld, J.F.; Slatkin, D.N.; Focella, T.M.; Smilowitz, H.M. Gold nanoparticles: A new X-ray contrast agent. *Br. J. Radiol.* **2006**, *79*, 248–253.
82. Ghazanfari, A.; Jung, K.-H.; Park, J.A.; Marasini, S.; Ho, S.L.; Miao, X.; Ahmad, M.Y.; Yue, H.; Yang, S.; Chae, K.S.; Chang, Y; Lee, G.H. Size-controlled one-pot polyol synthesis and characterization of D-glucuronic acid-coated ultrasmall BiOI nanoparticles as potential x-ray contrast agent. *Mater. Res. Express* **2018**, *6*, 015039.
83. Kandanapitiye, M.S.; Gao, M.; Molter, J.; Flask, C.A.; Huang, S.D. Synthesis, Characterization, and X-ray Attenuation Properties of Ultrasmall BiOI Nanoparticles: toward Renal Clearable Particulate CT Contrast Agents. *Inorg. Chem.* **2014**, *53*, 10189–10194.
84. Rabin, O.; Perez, J.M.; Grimm, J.; Wojtkiewicz, G.; Weissleder, R. An X-Ray Computed Tomography Imaging Agent Based on Long-Circulating Bismuth Sulphide Nanoparticles. *Nat. Mater.* **2006**, *5*, 118–122.
85. Brown, A.L.; Naha, P.C.; Benavides-montes, V.; Litt, H.I.; Goforth, A.M.; Cormode, D.P. Synthesis, X-ray Opacity, and Biological Compatibility of Ultra-High Payload Elemental Bismuth Nanoparticle X-ray Contrast Agents. *Chem. Mater.* **2014**, *26*, 2266–2274.
86. Swy, E.R.; Schwartz-Duval, A.S.; Shuboni, D.D.; Latourette, M.T.; Mallet, C.L.; Parys, M.; Cormode, D.P.; Shapiro, E.M. Dual-Modality, Fluorescent, PLGA Encapsulated Bismuth Nanoparticles for Molecular and Cellular Fluorescence Imaging and Computed Tomography. *Nanoscale* **2014**, *6*, 13104–13112.
87. Wei, B.; Zhang, X.; Zhang, C.; Jiang, Y.; Fu, Y.Y.; Yu, C.; Sun, S.K.; Yan, X.P. Facile Synthesis of Uniform-Sized Bismuth Nanoparticles for CT Visualization of Gastrointestinal Tract in Vivo. *ACS Appl. Mater. Interfaces* **2016**, *8*, 12720–12726.
88. Mao, F.; Wen, L.; Sun, C.; Zhang, S.; Wang, G.; Zeng, J.; Wang, Y.; Ma, J.; Gao, M.; Le, Z. Ultrasmall biocompatible Bi_2Se_3 nanodots for multimodal imaging-guided synergistic radiophotothermal therapy against cancer. *ACS Nano.* **2016**, *10*, 11145–11155.
89. Goldman, L.W. Principle of CT and CT technology. *J. Nucl. Med. Technol*. **2007**, *35*, 115–128.

90. Paeng, J.C.; Lee, D.S. Multimodal molecular imaging in vivo. *Open Nucl. Med. J*. **2010**, *2*, 145–152.
91. Currie, G.M. Pharmacology, part 5: CT and MRI contrast media. *J. Nucl. Med. Technol.* **2019**, *47*, 189–202.
92. Jain, P.K.; Huang, X.; El-Sayed, I.H.; El-Sayed, M.A. Noble Metals on the Nanoscale: Optical and Photothermal Properties and Some Applications in Imaging, Sensing, Biology, and Medicine. *Acc. Chem. Res*. **2008**, *41*, 1578–1586.
93. Vines, J.B.; Yoon, J.-H.; Ryu, N.-E.; Lim, D.-J.; Park, H. Gold nanoparticles for photothermal cancer therapy. *Front. Chem*. **2019**, *7*, 167.
94. Das, S.; Dowding, J.M.; Klump, K.E.; McGinnis, J.F.; Self, W.; Seal, S. Cerium oxide nanoparticles: applications and prospects in nanomedicine. *Nanomedicine* **2013**, 8, 1483–1508.
95. Black, J. Biological performance of tantalum. *Clin. Mater*. **1994**, *16*, 167–173.